Flow Turbulence Combust
DOI 10.1007/s10494-014-9529-5

The Effect of Pressure Gradient on Boundary Layer Receptivity

Mark W. Johnson · Ali Pinarbasi

Received: 25 March 2013 / Accepted: 10 January 2014
© Springer Science+Business Media Dordrecht 2014

Abstract This paper presents numerical results for the receptivity of three laminar boundary layers with zero (ZPG), adverse (APG) and favourable (FPG) pressure gradients. Each boundary layer is subjected to a series of simple freestream waveforms which can be considered as constituent parts of either an isotropic or a non-isotropic turbulent freestream. Each freestream waveform has a single frequency in each spatial direction and is divided into two mutually perpendicular components. The first component has a zero spanwise velocity and hence lies in the streamwise normal plane whereas the second component lies in a plane which is perpendicular both to this plane and the spatial frequency vector. High boundary layer receptivities are only obtained for a minority of these waveforms and so only the resulting flow structures for these waveforms are considered in detail. The dominant flow structures are identified as either Tollmien Schlichting (T-S) waves or streaky structures. The streaky structures can be induced by both freestream components, but the response to the second component, which results in streamwise vortices in the freestream, is considerably stronger and occurs over a much larger streamwise frequency range. The boundary layer is only receptive to a relatively narrow band of spanwise wavelengths ranging from approximately one to four times the local boundary layer thickness. The APG leads to receptivities which are more than double those for the FPG case. The ratio of the freestream fluctuation streamwise wavelength to the distance from the plate leading edge is identified as an important influential parameter for receptivity leading to streaks. Significant T-S activity is only observed for APG, but is also detected for ZPG.

Keywords Boundary layer · Transition · Receptivity

M. W. Johnson (✉)
School of Engineering, University of Liverpool, Liverpool L69 3GH, UK
e-mail: m.w.johnson@liv.ac.uk

A. Pinarbasi
Mechanical Engineering Department, Yildiz Technical University, 610 Istanbul, Turkey

Published online: 20 February 2014

Nomenclature

k	$= \frac{\nu}{U^2}\frac{dU}{dx}$ acceleration parameter
p	static pressure
p'	fluctuation pressure
R	receptivity (Eq. 30)
Re_x, Re_y, Re_z	$=\frac{U_0 x}{\nu}$, $\frac{U_0 y}{\nu}$, $\frac{U_0 z}{\nu}$ position Reynolds numbers
Re_{x0}	$= \frac{U_0 x_0}{\nu}$ leading edge Reynolds number
t	time
u, v, w	mean velocity components in x, y and z directions
u', v', w'	perturbation velocities in x, y and z directions
u_f, v_f, w_f	perturbation velocity amplitudes (Eq. 5)
U	mean freestream velocity
U'	$= \left(U_f^2 + V_f^2 + W_f^2\right)^{0.5}$ freestream velocity fluctuation amplitude
U_f, V_f, W_f	perturbation velocity amplitude components in freestream
x, y, z	streamwise, normal and spanwise co-ordinates
x_0	distance from turbulence generating grid to plate leading edge
β	turbulence decay constant (Eq. 24)
δ	boundary layer thickness
ω	temporal frequency
ω_x, ω_y, ω_z	spatial frequencies
Ω	$=\frac{\nu\omega}{U_0^2}$, dimensionless temporal frequency
Ω_x, Ω_y, Ω_z	$= \frac{\nu\omega_x}{U_0}$, $\frac{\nu\omega_y}{U_0}$, $\frac{\nu\omega_z}{U_0}$, dimensionless spatial frequencies
ν	fluid dynamic viscosity
ρ	fluid density

Subscripts

0	Value at turbulence generating grid
nw	near wall value $\left(\frac{y}{\delta} = 0.1\right)$

1 Introduction

The prediction of transition remains an important problem in many engineering applications and despite many years of research still remains largely reliant on empirical correlations obtained using wind tunnel data e.g., Abu-Ghannam and Shaw [1]. Many factors are known to affect the transition process (e.g., turbulence level, streamwise pressure gradient, sweep, concave curvature and turbulence length scale) but it is only possible to include the effects of perhaps two or three of these in a correlation if the number of experiments is to remain manageable. The lack of a universal transition model is therefore an obstacle to the accurate prediction of many engineering flows using CFD. A better understanding of transitional flows has been achieved over the past decade through DNS (e.g., Jacobs and Durbin [2]) and detailed experiments (e.g., Matsubara and Alfredsson [3], Mandal et al. [4] and Nolan and Walsh [5]), but a complete understanding is still illusive. Accurate prediction can be achieved using DNS, but DNS is prohibitively expensive as a design tool and is likely to remain so for more than a decade. If a complete understanding of the physics of transition can be found then it seems likely that a universal transition model can be developed which can be used within a RANS calculation.

The transition of an attached boundary layer from a laminar to a turbulent state is usually classified as either being through a natural mode or a bypass mode. Natural transition is the dominant mode for flows where the freestream turbulence level is less than about 1 % and therefore is the mode of relevance to aircraft structures, whereas bypass transition is the dominant mode for higher levels of freestream turbulence which occur within gas turbine engines, Morkovin [6]. Natural and bypass transition are usually treated as independent modes of transition, however in both cases the velocity perturbations which develop in the pre-transitional boundary layer can be predicted using linear perturbation theory. In natural transition, the development of the two dimensional T-S waves is only the first stage of the transition process, which is followed by the emergence of three dimensional structures. In bypass transition, only the streaky structures (or Klebanoff modes) are observed through flow visualisation experiments, but T-S activity is apparent from spectral analysis particularly for adverse pressure gradients on compressor blades (Hughes and Walker [7] and Zaki et al. [8].

For low Reynolds numbers, below the critical value required for T-S instability, only bypass modes will be present, however it seems likely that for freestream turbulence levels close to 1 %, where the Reynolds number will be above that required for T-S instability, both the T-S and streaky structure modes will exist and play an important role in the transition process. Numerical (Liu et al. [9] and Fasel [10]) and experimental work (Fransson et al. [11]) has been performed where the interaction of these two modes in zero pressure gradient boundary layers has been studied. Goldstein and Sescu [12] and Vaughan & Zaki [13] have also demonstrated that the presence of unsteady streaks leads to discrete instability modes which are highly unstable.

T-S waves and streaky structures can be thought of as analogous to the free and forced vibrations of a mechanical system, Zaki and Durbin [14, 15]. T-S waves result from instability and hence adopt the natural resonant frequency for the boundary layer and grow exponentially when damping is insufficient (i.e. once the critical Reynolds number is exceeded). On the other hand, bypass fluctuations within the boundary layer are forced by the freestream fluctuations and have an amplitude directly proportional to the amplitude of the freestream forcing (Johnson and Ercan [16] and Andersson et al [17]).

The theory for T-S waves which form in the first stage of natural transition was derived by Tollmien [18], before the first experimental observations were made by Schubauer and Skramstad [19] some 70 years ago. Theoretical techniques to predict the formation of the boundary layer streaky structures or Klebanoff modes resulting from the freestream velocity fluctuations are more complex and have only appeared much more recently. This is because T-S waves are 2-dimensional in nature whereas the mechanisms leading to streaky structures are 3-dimensional. Interpretation of experimental observations of T-S waves is also more straightforward as normally a single frequency is dominant. In contrast, the streaky structures observed in laminar boundary layers upstream of bypass transition contain many frequencies. There are two approaches which have been developed to predict the streaky structures in the boundary layer resulting from freestream fluctuations.

The first approach uses the Orr-Sommerfeld and Squire equations to determine the inlet fluctuation boundary condition within the laminar boundary layer. The Navier-Stokes equations are then solved downstream where full account of the non-parallel and non-linearity of the flow is made. Luchini [20] and Andersson et al. [17] used this form of analysis, and more recently the approach has also been used by Jacobs and Durbin [2], Schlatter et al. [21], Liu et al. [22], Zaki and Durbin [15] and Templemann et al. [23]. A second approach used by Leib et al. [24] and Ricco and Wu [25] uses the boundary region equations to determine the streaky boundary layer response to freestream fluctuations. Beyond the amplification of

streaks, secondary instability of the streaky flow ensues downstream and can be triggered by two mechanisms, one near the edge of the boundary layer and the other close to the wall (Vaughan and Zaki [13]).

The current work considers linear perturbations of the full Navier Stokes equations (i.e. linear DNS). The method is therefore equivalent to full DNS providing the perturbations to the boundary layer and freestream remain small. The results are therefore only valid in the pre-transitional boundary layer prior to the onset of secondary instability and the development of significant Reynolds stresses. Although a linear perturbation approach is used, none of the further approximations adopted in other work to simplify the analysis such as parallel flow or asymptotic limits are made. Thus the methodology can be used for completely general geometries and offers an alternative to expensive DNS calculations for the prediction of receptivity in pre-transitional boundary layers. The objective of the work was to study the response of the laminar boundary layer to general three dimensional freestream disturbances and hence to identify those disturbances which dominate the receptivity process and hence initiate transition. Unlike previous research work, which has predominantly concentrated on zero pressure gradient boundary layers, an objective of the current work was to consider how a streamwise favourable (FPG) or an adverse pressure gradient (APG) alter the boundary layer response to freestream fluctuations.

2 Theory

Receptivity is the process by which freestream velocity fluctuations induce fluctuations within the boundary layer. If these velocity fluctuations remain small compared with the mean velocity, the second order terms due to the products of the fluctuation terms can be neglected and hence the fluctuations can be treated as a linear perturbation to the mean flow. This approximation is justified as the second order or Reynolds stress terms are negligibly small for the pre-transitional boundary layer.

2.1 Mean flow

The geometry used for both the mean and perturbation computations is shown in Fig. 1. This consists of a plate of infinitesimal thickness with a chord Reynolds number $\mathrm{Re}_x = 525{,}000$ for the ZPG case. The APG and FPG were imposed by altering the boundary condition along the upper and lower flow domain boundaries, such that the freestream velocity varies linearly along the central portion of the plate from x = 58 to 442 mm. A zero pressure gradient was therefore maintained along a short length of the plate close to the leading edge x < 58 mm and trailing edge x > 442 mm. The freestream velocity decreases by 10 % along the central plate section for the APG and increases by 25 % for the FPG. The linear variation in velocity leads to an approximately constant value for the acceleration parameter k of -2.8 $\times$ 10^{-7} decreasing to -3.4 $\times$ $10^{-7}$for the APG and 6.9 $\times$ 10^{-7}decreasing to 4.4

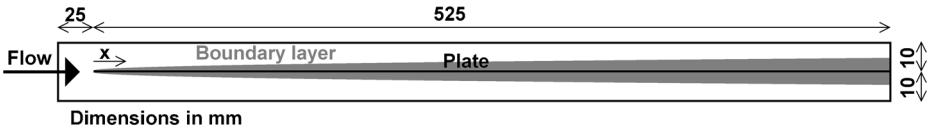


Fig. 1 Flat plate geometry used for the boundary layer calculations. The shaded area shows the zero pressure gradient boundary layer

$\times 10^{-7}$for the FPG along the central portion of the plate. The mean incompressible flow was calculated using a fourth order finite volume code on a regular rectangular mesh of 1x0.05 mm cells with 550 cells and 400 cells in the x and y directions respectively. A fourth order accurate finite volume numerical formulation with cell centre storage for all variables is used. Solution is achieved using an explicit second order time marching procedure with iterative pressure correction to solve the continuity equation at each time step.

The development of the three boundary layers (ZPG, APG and FPG) considered in this paper are shown in Fig. 2. The results for the ZPG case were validated through comparison with the Blasius solution. The laminar boundary layer develops to a final $Re_\theta = 477$ which is 0.9 % lower than the value for a Blasius boundary layer and the shape factor is within 1 % of the Blasius value over all but the first 10 % of the plate. Bypass transition occurs for turbulence levels less than 1 % where start of transition occurs at $Re_\theta = 400$ (Mayle [26]) and so this boundary layer is typical of laminar boundary layers pre bypass transition and hence is appropriate for the current receptivity study. The three boundary layers develop identically up to $Re_x = 80{,}000$ ($Re_\theta = 185$) prior to the start of the streamwise pressure gradient. Boundary layer profiles for the APG and FPG cases are plotted in Fig. 3. For the APG case, the boundary layer almost reaches separation ($H = 3.27$, $Re_\theta = 450$) at $Re_x = 326{,}000$ before recovering towards a zero pressure gradient profile ($H = 2.84$) at $Re_x = 417{,}000$ ($Re_\theta = 500$). Conversely for the FPG case, the shape factor decreases to $H = 2.31$ at $Re_x = 456{,}000$ ($Re_\theta = 350$) before recovering to $H = 2.46$ at $Re_x = 572{,}000$ ($Re_\theta = 400$).

2.2 Perturbed flow

If each flow quantity consists of a mean component and a perturbation then the resulting terms in the equations of motion will be zeroth, first or second order in the perturbation.

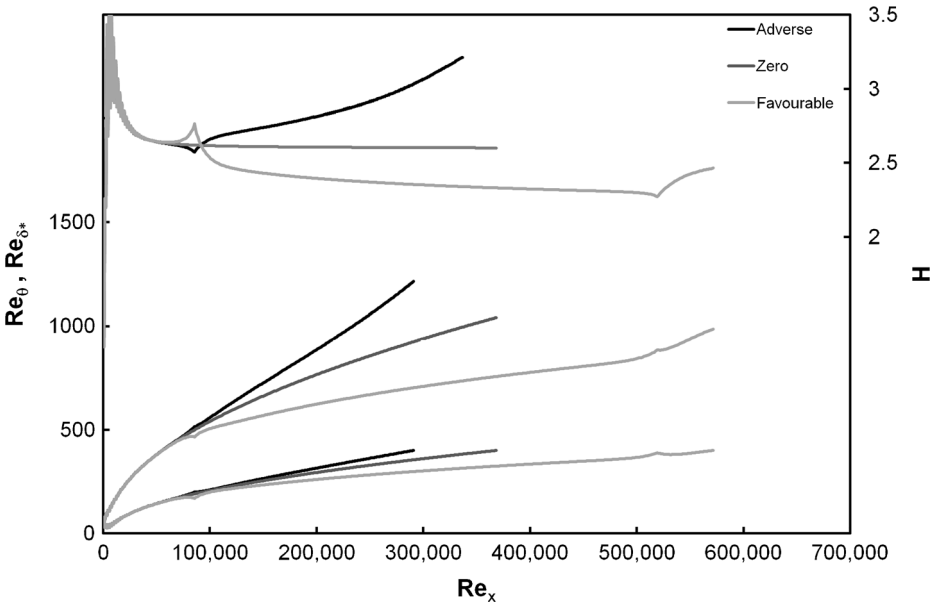


Fig. 2 Development of the laminar boundary layers

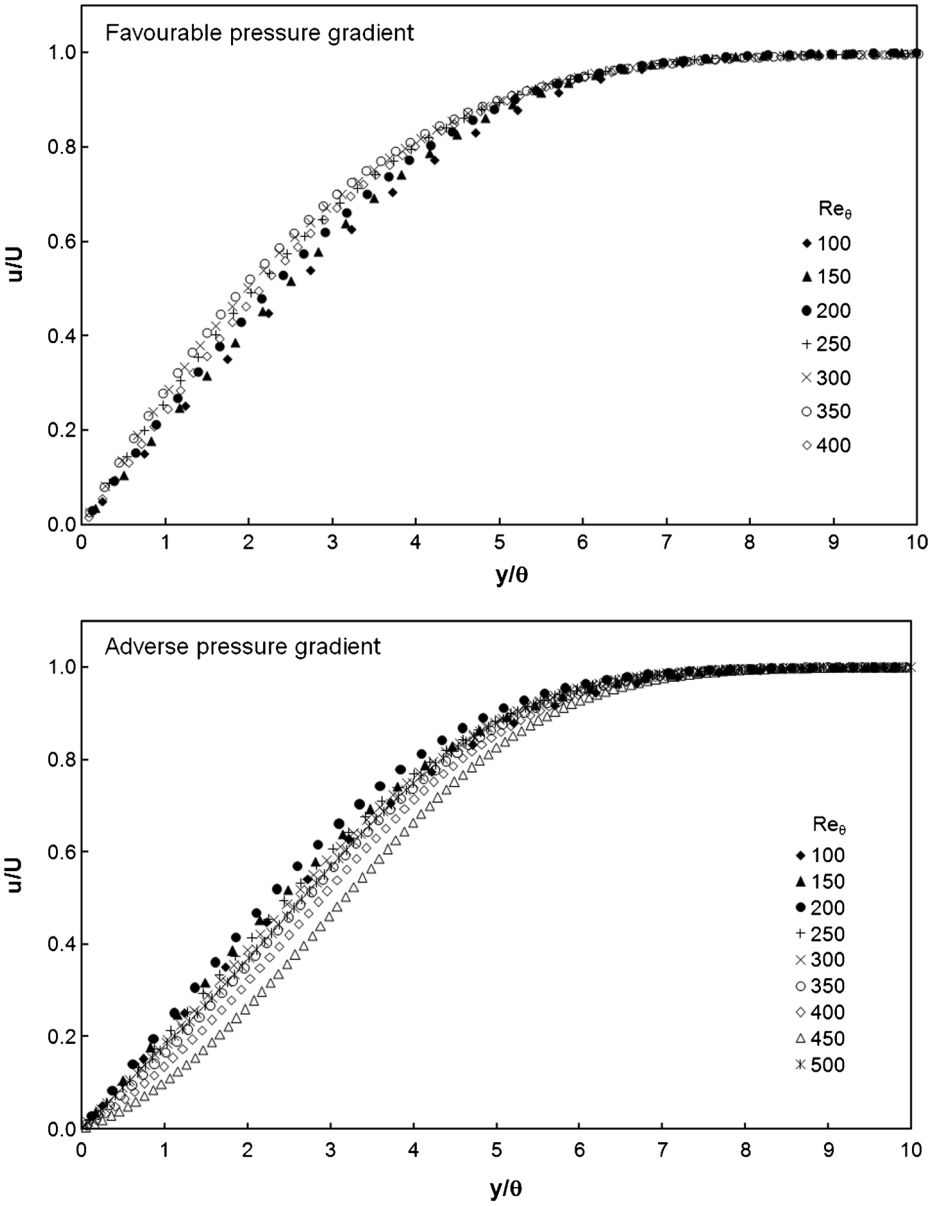


Fig. 3 Boundary layer profiles for the FPG and APG cases

The second order terms consist only of the Reynolds stress terms and these second order terms are neglected for the laminar flows being considered here. The perturbed flow is therefore restricted to a linear perturbation of the mean flow and is governed by the linearised unsteady Navier Stokes equations. The equations are the continuity equation

$$\frac{\partial u'}{\partial x} + \frac{\partial v'}{\partial y} + \frac{\partial w'}{\partial z} = 0 \tag{1}$$

and the momentum equations in the streamwise x, normal y and spanwise z, directions

$$\frac{\partial u'}{\partial t} + \frac{\partial}{\partial x}\left(\frac{p'}{\rho} + 2uu'\right) + \frac{\partial}{\partial y}\left(vu' + uv'\right) + \frac{\partial}{\partial z}\left(uw'\right) - \nu\nabla^2 u' = 0 \tag{2}$$

$$\frac{\partial v'}{\partial t} + \frac{\partial}{\partial x}\left(vu' + uv'\right) + \frac{\partial}{\partial y}\left(\frac{p'}{\rho} + 2vv'\right) + \frac{\partial}{\partial z}\left(vw'\right) - \nu\nabla^2 v' = 0 \tag{3}$$

$$\frac{\partial w'}{\partial t} + \frac{\partial}{\partial x}\left(uw'\right) + \frac{\partial}{\partial y}\left(vw'\right) + \frac{\partial}{\partial z}\left(\frac{p'}{\rho}\right) - \nu\nabla^2 w' = 0 \tag{4}$$

noting that, as the mean flow is two dimensional w and the z derivatives of u, v and p are zero. These equations are therefore the same as the linearised Navier Stokes equations used by Leib et al. [24] and others but retain the streamwise derivatives in the mean velocity.

The variation in the flow perturbations can be considered as periodic in time and also in the spanwise direction as the mean flow is invariant in this direction and so

$$u' = u_f\,(x,\,y)\,e^{i(\omega_z z + \omega t)} \tag{5}$$

with similar expressions for v', w'and p'. The equations can then be written as

$$\frac{\partial u_f}{\partial x} + \frac{\partial v_f}{\partial y} + i\omega_z w_f = 0 \tag{6}$$

$$i\omega u_f + \frac{\partial}{\partial x}\left(\frac{p_f}{\rho} + 2uu_f\right) + \frac{\partial}{\partial y}\left(vu_f + uv_f\right) + \omega_z u w_f - \nu\nabla^2 u_f + \nu\omega_z^2 u_f = 0 \tag{7}$$

$$i\omega v_f + \frac{\partial}{\partial x}\left(vu_f + uv_f\right) + \frac{\partial}{\partial y}\left(\frac{p_f}{\rho} + 2vv_f\right) + \omega_z v w_f - \nu\nabla^2 v_f + \nu\omega_z^2 v_f = 0 \tag{8}$$

$$i\omega w_f + \frac{\partial}{\partial x}\left(uw_f\right) + \frac{\partial}{\partial x}\left(vw_f\right) + \frac{\partial}{\partial z}\left(\frac{p_f}{\rho}\right) - \nu\nabla^2 w_f + \nu\omega_z^2 w_f = 0 \tag{9}$$

2.3 Boundary conditions

At the inlet, a boundary condition must be specified which represents the perturbed flow in the freestream. This boundary condition must be a solution of the set of equations just derived, simplified for the uniform freestream inlet flow u = U and v = 0. These simplified momentum equations are

$$i\omega u_f + \frac{\partial}{\partial x}\left(\frac{p_f}{\rho} + U u_f\right) - \nu\nabla^2 u_f + \nu\omega_z^2 u_f = 0 \tag{10}$$

$$i\omega v_f + \frac{\partial}{\partial x}\left(U v_f\right) + \frac{\partial}{\partial y}\left(\frac{p_f}{\rho}\right) - \nu\nabla^2 v_f + \nu\omega_z^2 v_f = 0 \tag{11}$$

$$i\omega w_f + \frac{\partial}{\partial x}\left(U w_f\right) + \frac{\partial}{\partial z}\left(\frac{p_f}{\rho}\right) - \nu\nabla^2 w_f + \nu\omega_z^2 w_f = 0 \tag{12}$$

Equations 10, 11 and 12 can be combined to eliminate the velocity components u_f, v_f and w_f resulting in

$$\nabla^2 p_f = 0 \tag{13}$$

Freestream turbulence consists of spatially and temporally periodic waveforms which decay in the streamwise direction and satisfy the flow equations. The freestream solution of the current equations at the inlet must therefore be of the form

$$u' = u_1 e^{i(\omega_x x+\omega_y y+\omega_z z+\omega t)-\beta x} \tag{14}$$

$$v' = v_1 e^{i(\omega_x x+\omega_y y+\omega_z z+\omega t)-\beta x} \tag{15}$$

$$w' = w_1 e^{i(\omega_x x+\omega_y y+\omega_z z+\omega t)-\beta x} \tag{16}$$

$$p' = p_1 e^{i(\omega_x x+\omega_y y+\omega_z z+\omega t)-\beta x} \tag{17}$$

Substituting for p' in Eq. 13

$$\beta^2 - \omega_x^2 - \omega_y^2 - \omega_z^2 - 2i\beta\omega_x = 0 \tag{18}$$

It therefore follows from Eq. 17 that if ω_x and β are non zero, $p_1 = 0$.

The freestream solution of these equations is therefore

$$u_f = u_1 e^{i(\omega_x x+\omega_y y)-\beta x} \tag{19}$$

$$v_f = v_1 e^{i(\omega_x x+\omega_y y)-\beta x} \tag{20}$$

$$w_f = w_1 e^{i(\omega_x x+\omega_y y)-\beta x} \tag{21}$$

$$p_f = 0 \tag{22}$$

This freestream solution is therefore a travelling wave with spatial frequencies ω_x, ω_y and ω_z which decays in the streamwise direction at a rate β. It should be noted that although there are no pressure fluctuations present in the freestream, pressure fluctuations are induced in the boundary layer by the freestream velocity fluctuations.

Substituting these expressions into any one of the momentum equations and equating the real and imaginary parts also provides a relationship between the streamwise spatial and temporal frequencies

$$\omega = -(U + 2\beta\nu)\,\omega_x \tag{23}$$

and an expression for the streamwise decay rate

$$\beta = -\frac{U}{2\nu} + \left(\left(\frac{U}{2\nu}\right)^2 + \omega_x^2 + \omega_y^2 + \omega_z^2\right)^{0.5} \tag{24}$$

or

$$\beta x = -\frac{Re_x}{2} + \frac{Re_x}{2}\left(1 + 4\left(\Omega_x^2 + \Omega_y^2 + \Omega_z^2\right)\right)^{0.5} \tag{25}$$

where $\Omega_x = \frac{\nu\omega_x}{U_0}$, $\Omega_x = \frac{\nu\omega_y}{U_0}$ and $\Omega_x = \frac{\nu\omega_z}{U_0}$

Typically in engineering problems

$$\Omega_x^2 + \Omega_y^2 + \Omega_z^2 << 1 \tag{26}$$

and so

$$\beta x \approx Re_x\left(\Omega_x^2 + \Omega_y^2 + \Omega_z^2\right) \tag{27}$$

These relationships indicate that, for a uniform mean flow, the freestream perturbation is convected at a velocity slightly greater than the freestream velocity and decays in proportion to ν and approximately in proportion to the square of the overall spatial frequency

$$\Omega_x^2 + \Omega_y^2 + \Omega_z^2 \tag{28}$$

The amplitudes of the velocity fluctuations, u_1, v_1 and w_1 must also satisfy the continuity equation and so

$$(i\omega_x - \beta)\, u_1 + i\omega_y v_1 + i\omega_z w_1 = 0 \tag{29}$$

The velocity vector must therefore lie in a plane which is perpendicular to the frequency vector$\left(i\omega_x - \beta, i\omega_y, i\omega_z\right)$. In the current work, this velocity vector is divided into two mutually perpendicular components. The first component is in the X-Y plane and hence has a zero component in the Z direction ($w_f = 0$) and lies in the same plane as the mean flow velocity. The second component is then perpendicular to this first component and the frequency vector and hence is in the direction with the maximum w_f component. Any general velocity vector can then be formed as a weighted average of these two components. It should be noted that although the freestream fluctuation velocity vector for a single component or a combination of components lies within a plane, the fluctuation velocities induced within the boundary layer do not lie in a plane and are fully 3-d in nature. An appropriately weighted combination of the two components over a complete range of Ω_x,Ω_y,$\Omega_z$spatial frequencies will result in the receptivity solution for isotropic turbulence in the freestream. It should also be noted that the combination of a solution with its 'mirror', where one of the spatial frequencies reverses sign, will result in an array of vortices in the freestream which are frequently used in receptivity studies. Equations 19, 20 and 21 are used to determine the velocities on the inlet boundary for each individual frequency solution where the values of u_1, v_1 and w_1 satisfy Eq. 29.

The remaining boundary conditions are more straightforward. On the plate the usual no slip boundary condition is used. The fluctuating pressure is set to zero on the boundaries parallel to and downstream of the plate, which is consistent with the freestream fluctuating velocity condition used at the inlet and the freestream solution. This pressure boundary condition differs from the velocity fluctuation condition used in other work (e.g., Leib et al. [24]), however the resulting velocity fluctuations in the freestream will be the same. This is because the velocity fluctuations prescribed at the inlet are convected through the boundaries where the zero pressure fluctuation boundary condition is used.

2.4 Validation

The perturbation Eqs. 6–9 were solved using a 4th order finite volume scheme and a similar solution procedure to that used for the mean flow. The same computational mesh was also used for mean and perturbed flows. A validation check was made for the freestream solutions to ensure that the 4^{th} order scheme and computational grid could accurately convect the fluctuation waveforms without significant artificial dissipation. Calculations were performed using the computational mesh for the mean boundary layer flow but with the plate removed and hence using a uniform mean flow. The frequency ranges considered, which were also used later for the receptivity study, were 10^{-6} and 10^{-3} for Ω_x and 3×10^{-5} and 3×10^{-3} for Ω_y and Ω_z. Figure 4 shows results where Ω_x, Ω_y and Ω_z were each varied with the frequencies in the other two directions held at their lowest value. The results in the figure show the error in the decay rate β when compared with the theoretical value given by Eq. 24. The figure indicates that the error increases substantially for higher Ω_x frequencies whilst the error remains small for high frequencies in the y and z directions. The reason for

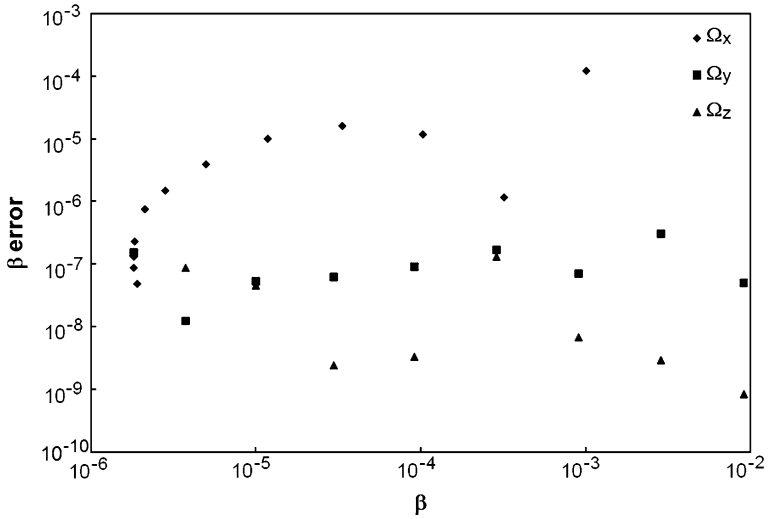


Fig. 4 Error in the decay rate of the freestream waveforms

this is that the grid size in the x direction is much larger than in the y direction. The Fourier representation in the z direction also leads to negligible numerical dissipation. The error in β is largest for the highest Ω_x and results in an additional 6.6 % decrease in the wave amplitude due to the numerical dissipation over the length of the plate. For all other frequencies the additional waveform decay due to numerical dissipation is less than 1 % and hence was considered to be negligible.

2.5 Perturbation solutions

Calculations were performed to obtain the first and second component solutions for 1053 ($= 13 \times 9 \times 9$) different frequency combinations. The frequencies were those used for the validation and are logarithmetrically distributed between 10^{-6} and 10^{-3} for Ω_x and 3×10^{-5} and 3×10^{-3} for Ω_y and Ω_z. The x frequency wavelengths range from 0.01 to 10 times the plate length and the y and z frequencies from approximately 0.5 to 50 times the boundary layer thickness at the plate trailing edge. The amplitude of the lowest frequencies will decay by only 0.1 % over the length of the plate whereas the amplitude of the highest frequencies will decay by a factor of 20,000. The calculations were performed simultaneously for the boundary layers on the upper and lower sides of the plate (see Fig. 1). The waves therefore impact the boundary layer at an acute angle on the upper surface and an oblique angle on the lower surface and hence the solutions for the two boundary layers are not identical. Solutions for the boundary layer on the lower surface are equivalent to those which would have been obtained on the upper surface if a negative Ω_y had been used and so are identified as such in the results. The solutions are used to identify the frequencies of the most receptivity modes. This is assessed by determining the receptivity coefficient R, which is here defined as the ratio between the near wall turbulence level and that at the turbulence generating location (or grid).

$$R = \left(\frac{u_f}{u}\right)_{nw} \frac{U}{U_{f0}} \tag{30}$$

The near wall turbulence level $\left(\frac{u_f}{u}\right)_{nw}$ is determined at a position in the boundary layer where $\frac{y}{\delta} \approx 0.1$. This is within the near wall region, which extends from the wall to approximately $\frac{y}{\delta} = 0.2$. Johnson and Ercan [16] found, in their experiments, that $\frac{u_f}{u}$ is approximately constant throughout the near wall region and so the exact position chosen when determining the receptivity is not critical. This was confirmed for the current results as shown in Fig. 5 where the receptivity to a typical second component velocity perturbation is plotted against distance from the wall. In Eq. 30, $U_{f0} = \frac{\left(u_1^2+v_1^2+w_1^2\right)^{0.5}}{3}$ is the freestream fluctuation velocity at the turbulence generating grid. In the current work, the turbulence grid is assumed to be located at a streamwise distance $x_0 = 500$ mm upstream of the plate leading edge such that $Re_{x_0} = \frac{Ux_0}{\nu} = 5x10^5$, which is typical of most laboratory wind tunnels. R therefore represents the amplitude of a particular frequency mode in the near wall spectrum if it is assumed that all frequency modes have an identical amplitude when they are created at the turbulence grid.

3 Results

The receptivity coefficients are compared for each of the 1053 ($13 \times 9 \times 9$) frequency modes for both the first and second component solutions at Re_θ increments of 50 along the plate for each pressure gradient. There are therefore 8, 9 and 10 Re_θ stations for the FPG, ZPG and APG cases respectively.

In order to compare the receptivities for the different pressure gradients, the results are presented for the station where $Re_\theta = 350$ where the shape factors are H = 2.31, 2.60 and

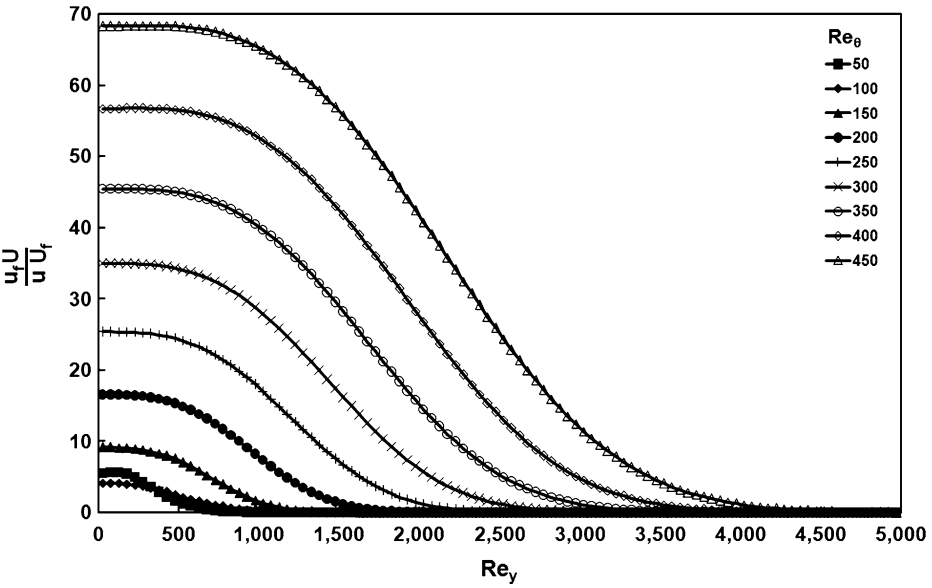


Fig. 5 Receptivity variation with distance from the wall for a second component freestream fluctuation with $\Omega_x = 10^{-6}$, $\Omega_y = 5.3 \times 10^{-4}$ and $\Omega_z = 5.3 \times 10^{-4}$

2.87 for the FPG, ZPG and APG respectively. The first component and second component solutions will be considered separately.

3.1 First component solutions

Figure 6 shows the iso-surfaces for a receptivity of 8 in the spatial frequency domain for the first component waves at $\mathrm{Re}_\theta = 350$. There is one region of high receptivity which is common to all pressure gradients which occurs at approximately $\Omega_x = 10^{-5}$, $\Omega_y = 3 \times 10^{-5}$ and $\Omega_z = 5.3 \times 10^{-4}$. A more detailed comparison is made in Fig. 7 where the variation with Ω_y and Ω_z frequencies is considered at a $\Omega_x = 10^{-5}$. The highest receptivities are achieved at the lowest Ω_y frequency of 3×10^{-5} and $\Omega_z = 5.3 \times 10^{-4}$ for all pressure gradients. For the ZPG and FPG the receptivities are almost identical for all Ω_y and Ω_z with a maximum receptivity of 25, but for APG this maximum is raised to 35 and the variation with Ω_y and Ω_z frequencies differs. Figure 7 also shows that the receptivities for negative Ω_y (boundary layer below the plate) are a little higher than for positive Ω_y(boundary layer above the plate) but overall the receptivities for negative and positive Ω_y are similar.

The streamwise fluctuating velocity boundary layer profiles at the nine streamwise stations are shown in Fig. 8 for the most receptive frequencies of $\Omega_x = 10^{-5}$, $\Omega_y = 3 \times 10^{-5}$ and $\Omega_z = 5.3 \times 10^{-4}$. Close to the wall the fluctuations increase linearly with distance from the wall, but then peak close to mid boundary layer height and then decrease towards the constant freestream value. The peak value also increases approximately linearly with Re_θ. A different behaviour is observed at $\mathrm{Re}_\theta = 50$ which is believed to be due to the proximity of the leading edge. The profile observed in Fig. 8 is qualitatively very similar to that observed in the experiments of Westin et al. [27] although their results were for a single temporal frequency and hence would be equivalent to a combination of many spatial frequencies from the current work.

Figure 7 indicates that the boundary layer is similarly receptive to spanwise wavelengths from at least δ to 4δ and hence the results suggest that the streaks observed in boundary layers subjected to freestream turbulence will exhibit a range of spanwise spacings. This spanwise spacing is consistent with experimental observations, e.g., Westin et al. [27]. For the single spatial frequencies considered here, the streamwise extent of the streaks will be equal to half the streamwise wavelength of $\mathrm{Re}_\lambda = 6.3 \times 10^5$ or about 60 % of the length of the plate. A superposition of all spatial frequencies though will lead to a much shorter observed length for individual streaks.

For the APG case a further region of high receptivity is observed at approximately $\Omega_x = 3.2 \times 10^{-4}$ in Fig. 6. This solution differs from the one already discussed in that the solution remains periodic in time, i.e. the solution has a temporal frequency content other than at the single frequency Ω given by Eq. 23. When the temporal evolution of the solution exhibiting the peak receptivity ($\Omega_x = 3.2 \times 10^{-4}$, $\Omega_y = 3 \times 10^{-3}$, $\Omega_z = 3 \times 10^{-3}$) was considered it was found that this solution has a temporal frequency which is less than Ω indicating that the fluctuations are moving downstream at less than the freestream velocity, which is a characteristic of T-S waves. Figure 9 shows how the peak u' fluctuation velocity in this APG boundary layer develops along the plate for this frequency case. There is an increase in the fluctuation level close to the leading edge, but this decays rapidly and the fluctuation level then remains close to that in the freestream until Re_x exceeds 200,000 ($\mathrm{Re}_\theta = 350$). At this point the Orr-Sommerfeld neutral stability loop is crossed and the T-S waves begin to grow rapidly with downstream distance. The fluctuations grow by a factor of approximately 1000 by the time the APG relaxes at $\mathrm{Re}_x = 374{,}000$ and the boundary layer profile recovers to a condition outside the stability loop leading to decay in the fluctuations. This result confirms

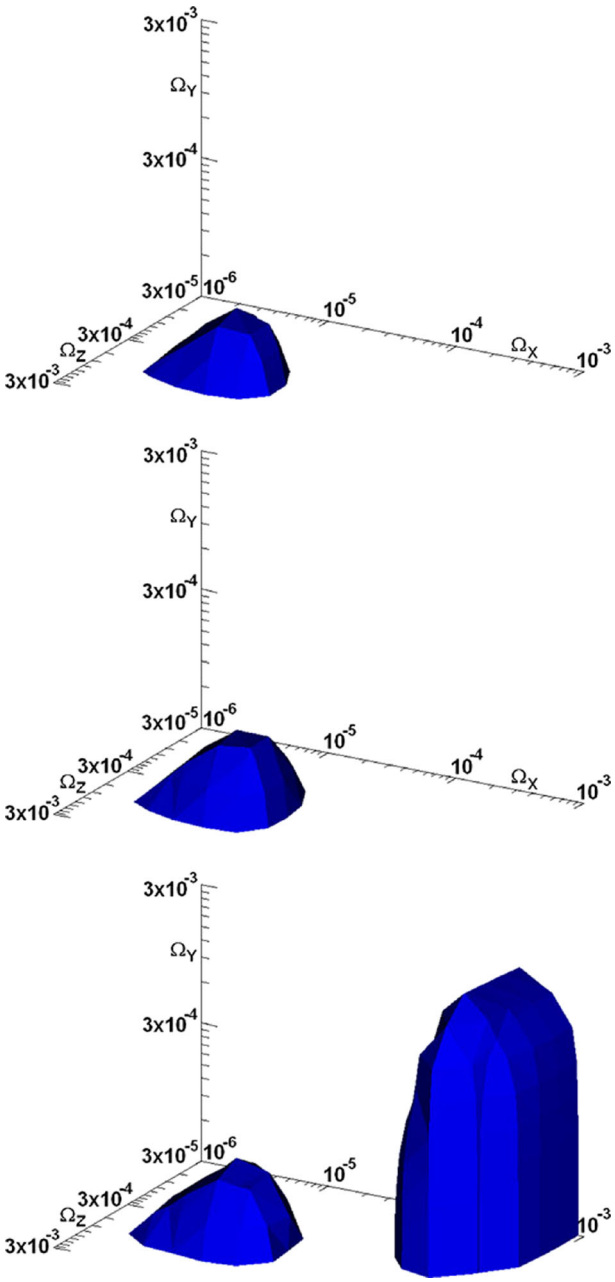


Fig. 6 Receptivity iso-surface of 8 for the first component fluctuations. ZPG (*top*), FPG (*middle*), APG (*bottom*)

the observation made in the experiments of Hughes and Walker [7] that TS waves are more prevalent for an APG than for ZPG and FPG. This has also been observed in the DNS results of Liu et al. [9] and Zaki et al. [8].

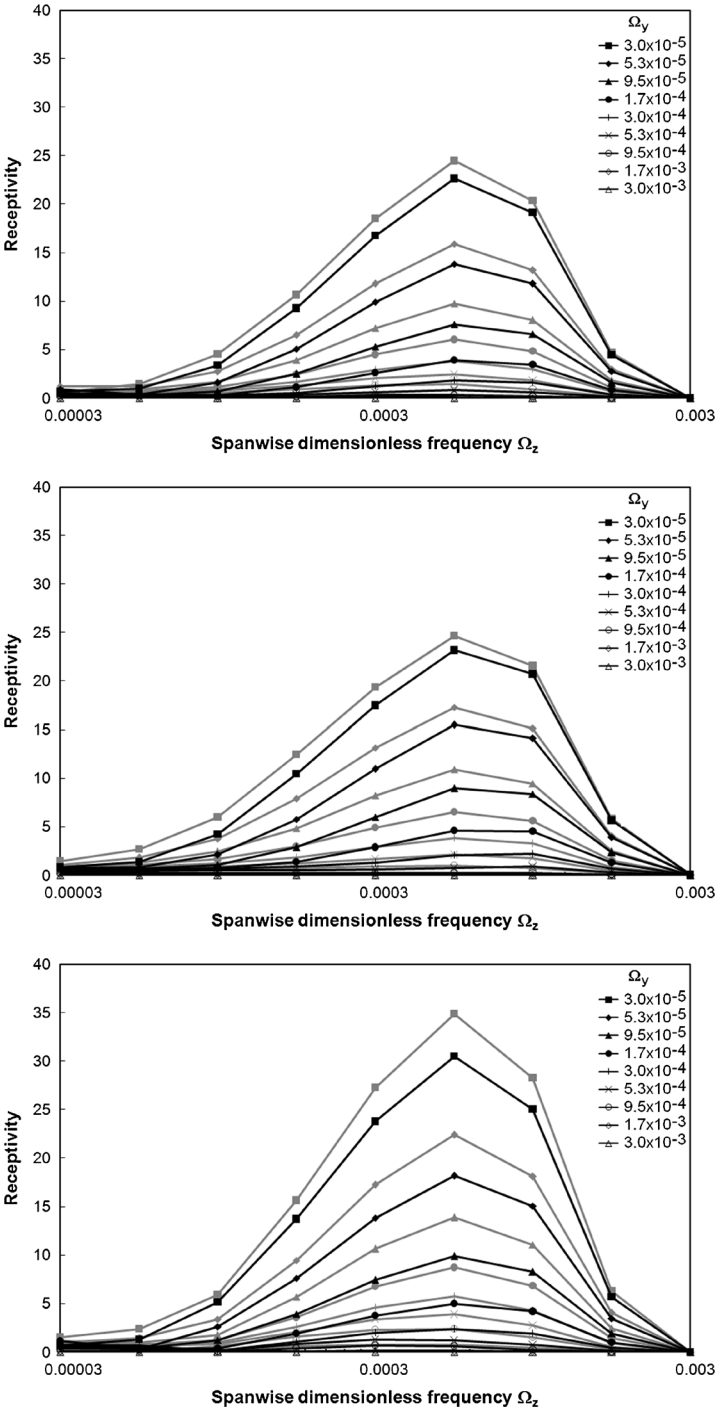


Fig. 7 First component perturbation receptivities for $\Omega_x = 10^{-5}$. ZPG (*top*), FPG (*middle*), APG (*bottom*). Black symbols +ve Ω_y and grey symbols –ve Ω_y

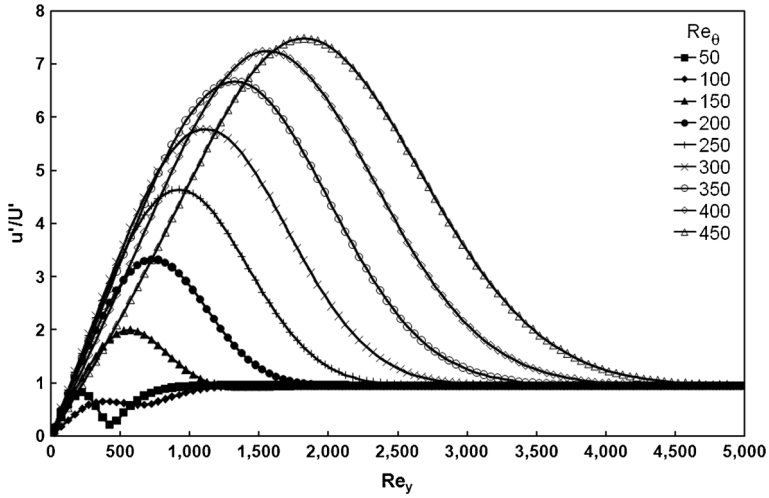


Fig. 8 First component streamwise perturbation velocities for $\Omega_x = 10^{-5}$, $\Omega_y = 3 \times 10^{-5}$ and $\Omega_z = 5.3 \times 10^{-4}$

3.2 Second component solutions

Figure 10 shows the iso-surface for a receptivity of 20 for the second component fluctuations and for each pressure gradient. There is a single region of high receptivity common to all pressure gradients which occurs at a similar $\Omega_z = 5.3 \times 10^{-4}$ to the first component high receptivity region in Fig. 6, however this region is larger than for the first component as it extends to the lowest Ω_x frequency. Figure 11 shows the receptivity variation at $\mathrm{Re}_\theta = 350$ for $\Omega_x = 10^{-6}$ which is broadly similar to the corresponding first component plot at the

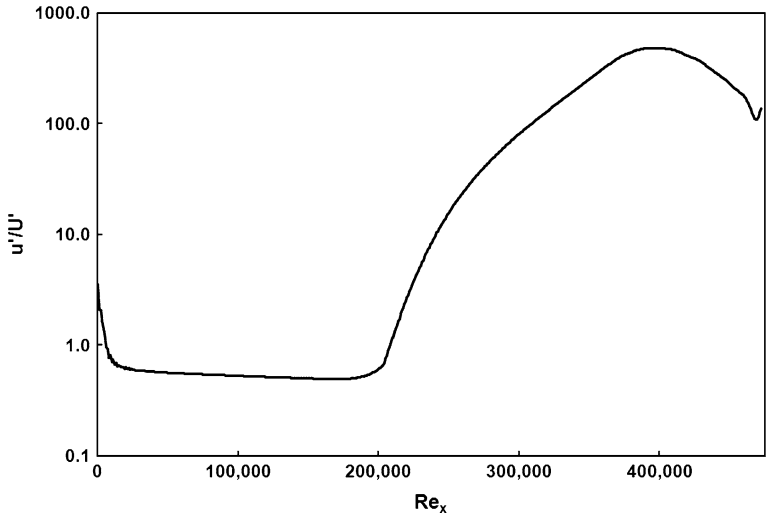


Fig. 9 First component maximum streamwise perturbation velocities for $\Omega_x = 3 \times 10^{-4}$, $\Omega_y = 3 \times 10^{-5}$ and $\Omega_z = 3 \times 10^{-5}$

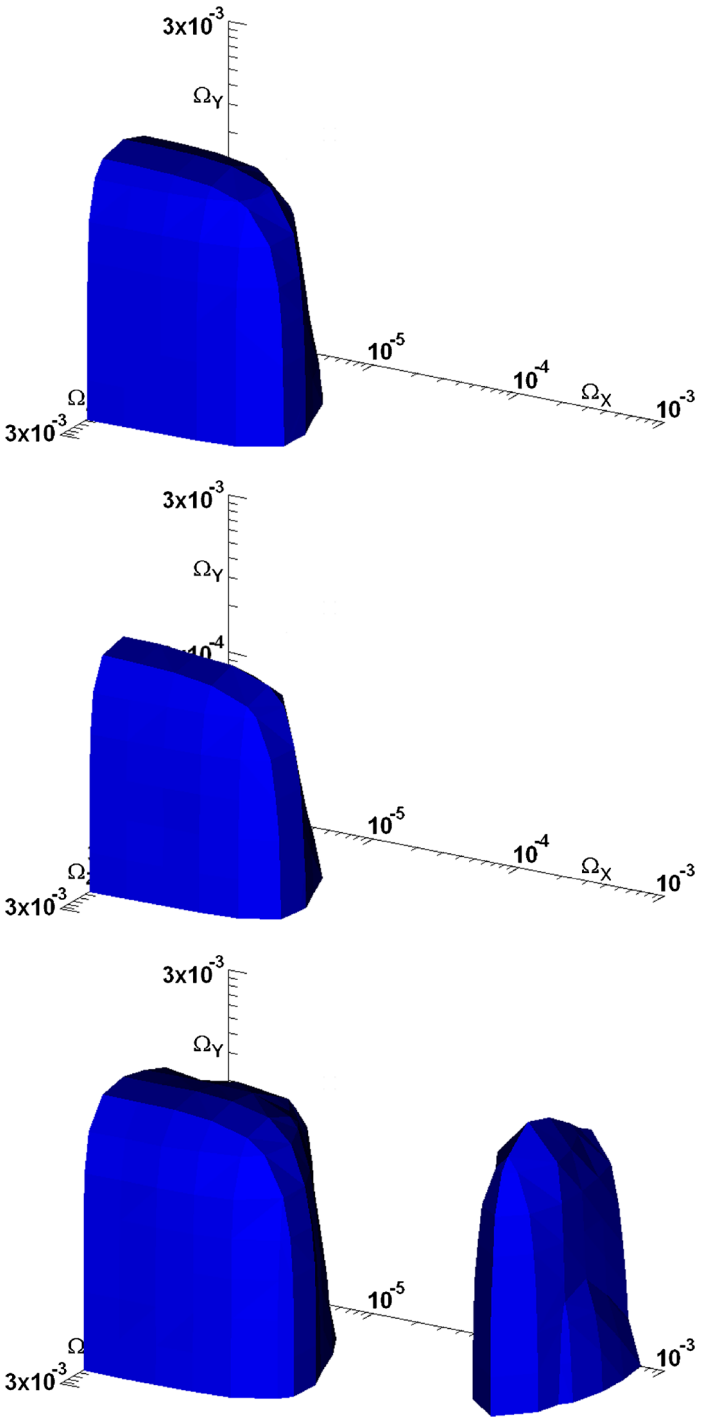


Fig. 10 Receptivity iso-surface of 20 for the second component fluctuations. ZPG (*top*), FPG (*middle*), APG (*bottom*)

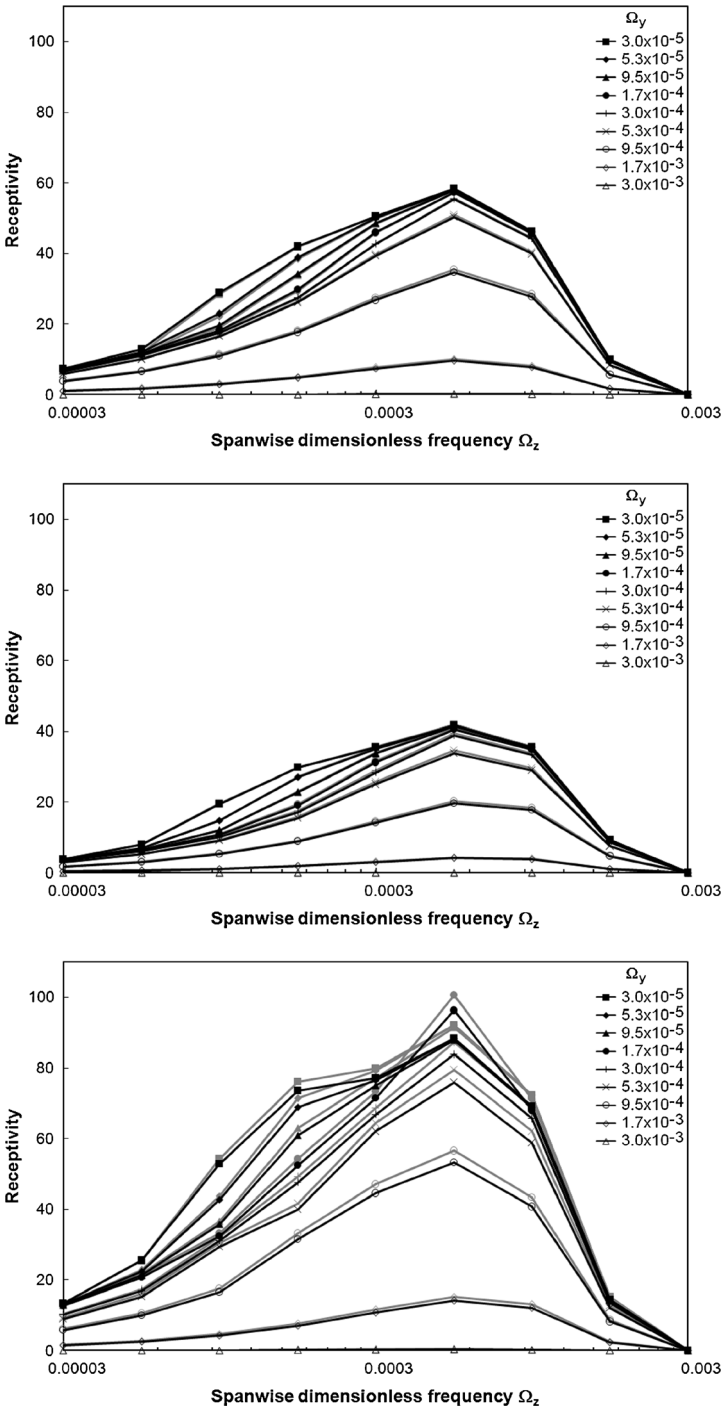


Fig. 11 Second component perturbation receptivities for $\Omega_x = 10^{-6}$. ZPG (*top*), FPG (*middle*), APG (*bottom*). Black symbols +ve Ω_y and grey symbols –ve Ω_y

higher $\Omega_x = 10^{-5}$ shown in Fig. 7. The receptivities for the second component are approximately twice the magnitude however and so it can be concluded that the second component plays a greater role in the transition process at this Re_θ. The difference between the negative and positive Ω_y frequencies (boundary layers below and above the plate) is much smaller for the second component than it was for the first component. The effect of pressure gradient on receptivity is also much greater for the second component where receptivity values for APG are typically double those for FPG, in comparison with the modest increase of about 40 % in receptivity for the first component.

The development of the streamwise fluctuating velocity profile for $\Omega_x = 10^{-6}$, $\Omega_y = 5.3 \times 10^{-3}$ and $\Omega_z = 5.3 \times 10^{-3}$ is plotted in Fig. 12. The profiles are similar to those for the first component except that the value decreases to zero in the freestream. This is because as Ω_x tends to zero compared with Ω_y and Ω_z the frequency vector tends to the streamwise direction and hence at this low Ω_x the second component fluctuations lie almost within the Y-Z plane. It should therefore be noted that the combination of this second component solution with a similar solution but with the sign of Ω_z reversed (i.e. $\Omega_z = -5.3 \times 10^{-3}$) would result in an array of streamwise vortices in the freestream. The frequency case plotted in Fig. 12 is for equal Ω_y and Ω_z frequencies, but similarly high receptivities for lower Ω_y frequencies are also obtained (see Fig. 11) and so similar boundary layer streaks can be induced by freestream streamwise vortices with aspect ratios up to at least 10.

The high receptivity frequency bands observed here are consistent with those obtained in the DNS performed by Jacobs and Durbin [2] and hence this result confirms that the current linear perturbation approach is able to return similar results for the pre-transitional boundary layer to a full DNS calculation. The fact that the non-linear terms do not play a significant role in the pre-transitional boundary layer also means that the perturbations within the boundary layer can be predicted for both isotropic and non-isotropic freestream turbulence through the superposition of a large number of individual frequency solutions.

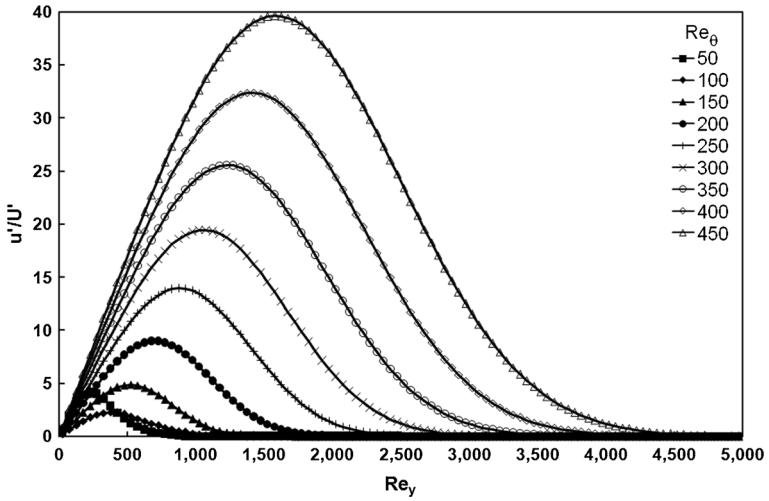


Fig. 12 Second component streamwise perturbation velocities for $\Omega_x = 10^{-6}$, $\Omega_y = 5.3 \times 10^{-4}$ and $\Omega_z = 5.3 \times 10^{-4}$

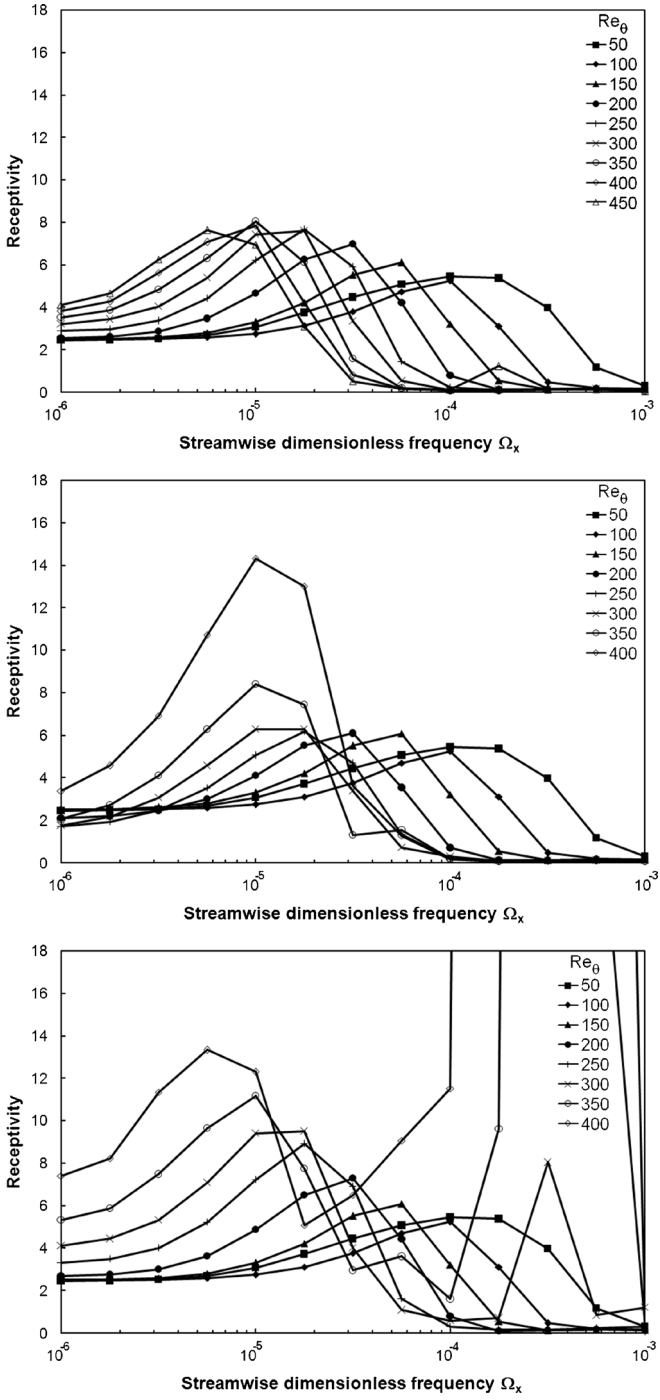


Fig. 13 Spanwise and wall normal averaged first component receptivities. ZPG (*top*), FPG (*middle*), APG (*bottom*)

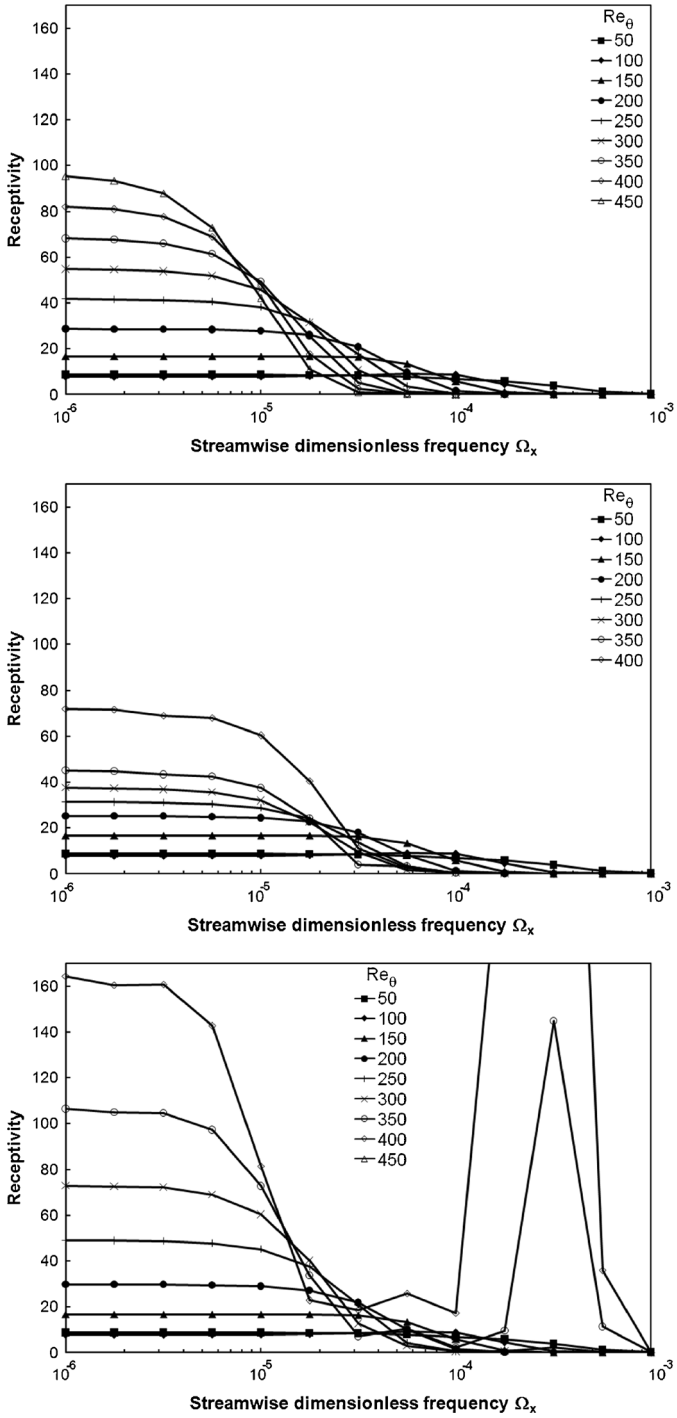


Fig. 14 Spanwise and wall normal averaged second component receptivities. ZPG (*top*), FPG (*middle*), APG (*bottom*)

3.3 Frequency averaged receptivities

The receptivity coefficient averaged over both the normal and spanwise frequencies for the first and second component solutions are plotted in Figs. 13 and 14 for each Re_θ and each pressure gradient. The receptivity for both first and second component fluctuations increases steadily with increasing Re_θ at low Ω_x ($< 10^{-5}$) but conversely decreases steadily for high Ω_x ($> 10^{-4}$) up to the onset of T-S instability for the APG case for $\mathrm{Re}_\theta > 200$. The more rapid decay of the freestream fluctuations with streamwise distance at higher Ω_x is largely responsible for the decrease in receptivity.

In the case of the first component fluctuations, the peak in receptivity moves to lower Ω_x with increasing Re_θ. Figure 15 shows that the maximum receptivity occurs when the distance from the plate leading edge is approximately half of the wavelength for the fluctuation frequency Ω_x. This suggests that for these long wavelengths the perturbation solution is essentially a progression through pseudo steady states where the fluctuations are caused by the changes in the global freestream conditions, i.e. the boundary layer is able to respond to the freestream changes with negligible phase lag. For the APG the largest contribution to the receptivity for $\mathrm{Re}_\theta > 200$ is from the T-S waves ($10^{-4} < \Omega_x < 3.2 \times 10^{-4}$) which grow rapidly in the streamwise direction. There is no evidence of T-S instability for the FPG case, but a peak is beginning to develop at $\Omega_x = 1.8 \times 10^{-4}$ for ZPG at $\mathrm{Re}_\theta = 450$.

The receptivities for the second component (Fig. 14) are typically an order of magnitude higher then for the first component. For $\Omega_x > 10^{-4}$, the receptivities are similar for the first and second components, however unlike the first component receptivities, the second component receptivities do not start to decrease once the half wavelength exceeds the distance from the plate leading edge, but rather tend to plateau towards a maximum value reached at the lowest Ω_x frequency. An explanation for this can be found by considering the mechanism for the streaky flow structure described earlier. The increase in receptivity with decreasing Ω_x is due to the fact that momentum is being added to the boundary layer by the downwash between adjacent freestream vortices over a longer streamwise length. However, the maximum length over which momentum can be added is the available upstream length

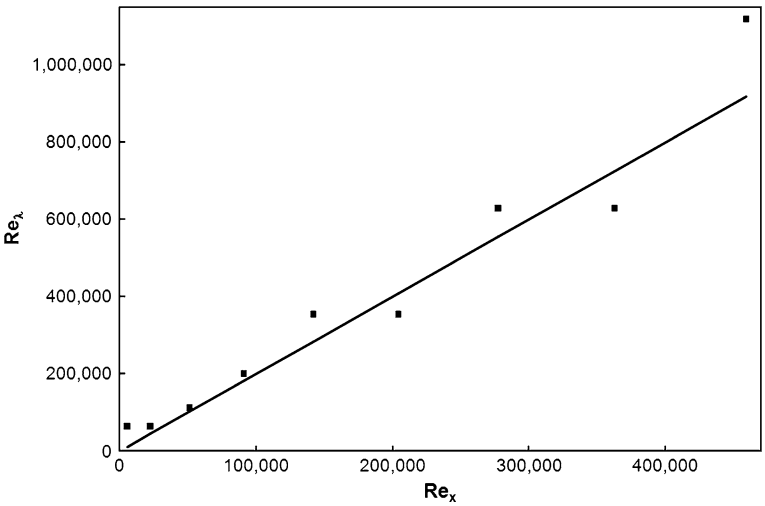


Fig. 15 Most receptive wavelength Reynolds number variation along the plate for the ZPG case

of the plate. The maximum receptivity therefore starts to plateau once the upstream length of plate available is less than approximately half of the fluctuation streamwise wavelength. It is also worth noting that the second component receptivity shows a strong dependence on the pressure gradient with a peak receptivity for APG more than double that for FPG.

The second component fluctuations are dominant in the receptivity process and hence this plot is qualitatively very similar to the measured values obtained through the spectral analysis of hot wire data by Johnson and Ercan [16]. It should be noted that here the variation with the spatial streamwise frequency Ω_x is considered whereas Johnson and Ercan's measurements considered the variation with the temporal frequency Ω, however Eq. 23 indicates that these frequencies are approximately equal for low frequency where the decay rate β is low.

Zaki and Durbin [14] also observed significantly higher receptivities with APG in their DNS, which is also consistent with the measured start of transition locations in APG experiments (e.g., Abu-Ghannam and Shaw [1]).

4 Conclusions

1. The effect of freestream waveforms of varying streamwise, normal and spanwise frequency within ZPG, APG and FPG boundary layers have been determined using a linear perturbation CFD approach. The freestream waveform for each set of spatial frequencies was divided into two mutually perpendicular components. Isotropic or non-isotropic freestream turbulence can be represented by weighted combinations of these two components over all possible spatial frequencies.
2. The boundary layer was found to be only receptive to a number of relatively narrow frequency bands. Two frequency regimes were identified that lead to receptivities greater than 20. The first of these is responsible for the generation of the alternating streaks of accelerated and decelerated fluid in the boundary layer commonly known as streaky structures. The second frequency regime is responsible for the generation of T-S waves.
3. The streaky structures are induced by freestream velocity fluctuations with a relatively narrow range of spanwise wavelengths from approximately δ to 4δ, but over a wide range of streamwise and wall normal wavelengths up to approximately double the distance from the plate leading edge and 2δ respectively. The boundary layer is most receptive to the second component freestream fluctuations which take the form of streamwise vortices. These vortices convect streamwise momentum to and from the boundary layer over prolonged streamwise distances and hence induce the streaks of increased and decreased streamwise velocity. First component freestream fluctuations in the form of spanwise vortices modulated at the most receptive spanwise wavelengths also contribute to the formation of the streaky structures, but the resulting streaks will have a shorter streamwise length. The boundary layer fluctuation profiles and streak spacing are consistent with other published work.
4. Significant T-S instability was only observed in the APG case for $Re_\theta > 200$, but some evidence was also observed in the ZPG case for $Re_\theta > 450$. This result was consistent with other published experimental and numerical work.
5. The receptivity was shown to be highly dependent on the ratio of the streamwise fluctuation wavelength and the distance from the leading edge λ/x. For the first component the maximum receptivity occurred when $\lambda/x = 0.5$ whereas for the second component a maximum receptivity plateau was reached when $\lambda/x > 0.5$ approximately.

6. The primary effect of changing from a FPG to an APG is to increase the receptivity to all spatial frequencies. The receptivity doubles for the second component waveforms whereas it only increases by about 40 % for the first component. Strong T-S waves are only seen for the APG boundary layer, but some T-S activity is apparent for ZPG.

5 Future Work

The current analysis is restricted to linear perturbations, however it should be noted that a complete non-linear analysis can be achieved simply by adding the second order velocity perturbation terms to Eqs. 2–4. These terms can be computed from the linear fluctuation terms and can be treated as a source term in the iterative solution of the equations. This would result in a full DNS, however the current computational grid is too coarse to resolve the resulting higher frequencies.

The current approach can also be extended to general geometries and so the receptivity of boundary layers on more realistic surfaces involving curvature and sweep can be studied.

References

1. Abu-Ghannam, B.J., Shaw, R.: Natural transition of boundary layers—the effects of turbulence, pressure gradient and flow history. J. Mech. Eng. Sci. **22**, 213–228 (1980)
2. Jacobs, R.G., Durbin, P.A.: Simulations of bypass transition. J. Fluid Mech. **428**, 185–212 (2001)
3. Matsubara, M., Alfredsson, P.H.: Disturbance growth in boundary layers subjected to free-stream turbulence. J. Fluid Mech. **430**, 149–168 (2001)
4. Mandal, A.C., Venkatakrishnan, L., Dey, J.: A study on boundary-layer transition induced by free-stream turbulence. J. Fluid Mech. **660**, 114–146 (2010)
5. Nolan, K.P., Walsh, E.J.: Particle image velocimetry measurements of a transitional boundary layer under free stream turbulence. J. Fluid Mech. **702**, 215–238 (2012)
6. Morkovin, M.V.: On the many faces of transition. In: Wells, C.S. (ed.) Viscous Drag Reduction, p. 412. Plenum, NY (1969)
7. Hughes, J.D., Walker, G.J.: Natural transition phenomena on an axial compressor blade. J. Turbomach. **123**, 392–401 (2001)
8. Zaki, T.A., Wissink, J.G., Rodi, W., Durbin, P.A.: Direct numerical simulation of transition in a compressor cascade: influence of free-stream turbulence. J. Fluid Mech. **665**, 57–98 (2010)
9. Liu, Y., Zaki, T.A., Durbin, P.A.: Boundary layer transition by interaction of discrete and continuous modes. J. Fluid Mech. **604**, 199–233 (2008)
10. Fasel, H.F.: Numerical investigation of the interaction of the Klebanoff-mode with a Tollmien-Schlichting wave. J. Fluid Mech. **450**, 1–33 (2002)
11. Fransson, J.H.M., Brandt, L., Talamelli, A., Cossu, C.: Experimental study of the stabilisation of Tollmein-Schlichting waves by finite amplitude streaks. Phys. Fluids, 17 (2005)
12. Goldstein, M.E., Sescu, A.: Boundary layer transition at high free-stream disturbance levels—beyond Klebanoff modes. J. Fluid Mech. **613**, 95–124 (2008)
13. Vaughan, N.J., Zaki, T.A.: Stability of zero-pressure-gradient boundary layer distorted by unsteady Klebanoff streaks. J. Fluid Mech. **681**, 116–153 (2011)
14. Zaki, T.A., Durbin, P.A.: Mode interaction and the bypass route to transition. J. Fluid Mech. **531**, 85–111 (2005)
15. Zaki, T.A., Durbin, P.A.: Continuous mode transition and the effects of pressure gradient. J. Fluid Mech. **563**, 357–388 (2006)
16. Johnson, M.W., Ercan, A.H.: A physical model for bypass transition. Int. J. Heat Fluid Flow **20**, 95–104 (1999)
17. Andersson, P., Berggren, M., Henningson, D.S.: Optimal disturbances and bypass transition in boundary layers. Phys. Fluids **11**, 134–150 (1999)
18. Tollmien, W. Uber die Entstehung der Turbulenz. 1 Mitteilung, nachr. Ges. Wiss. Gottingen. Math. Phys. Klasse 21–44, 1929; Engl. Transl. in NACA TM 609 (1931)

19. Schubauer, G.B., Skramstad, H.K.: Laminar boundary layer oscillations and stability of laminar flow. National Bureau of Standards Research Paper 1772, Reprint of Confidential NACA Report (1943)
20. Luchini, P.: Reynolds-number-independent instability of the boundary layer over a flat surface: optimal perturbations. J. Fluid Mech. **404**, 289–309 (2000)
21. Schlatter, P., Brandt, L., de Lange, H.C., Henningson, D.S.: On streak breakdown in bypass transition. Phys. Fluids **20** (2008). Article No. 101505
22. Liu, Y., Zaki, T.A., Durbin, P.A.: Floquet analysis of secondary instability of boundary layers distorted by Klebanoff streaks and Tollmien-Schlichting waves. Phys. Fluids **20** (2008). Article No. 124102
23. Templemann, D., Hanifi, A., Henningson, D.S.: Spatial optimal growth in three-dimensional compressible boundary layers. J. Fluid Mech. **704**, 251–279 (2012)
24. Leib, S.J., Wundrow, D.W., Goldstein, M.E.: Effect of free-stream turbulence and other vortical disturbances on a laminar boundary layer. J. Fluid Mech. **380**, 169–203 (1999)
25. Ricco, P., Wu, X.: Response of a compressible laminar boundary layer to free-stream vortical disturbances. J. Fluid Mech. **587**, 97–138 (2007)
26. Mayle, R.E.: The role of laminar-turbulent transition in gas turbine engines. ASME J. Turbomach. **113**, 509–537 (1991)
27. Westin, K.J.A., Boiko, A.V., Klingmann, B.G.B., Kozlov, V.V., Alfredsson, P.H.: Experiments in a boundary layer subjected to free stream turbulence. Part 1. Boundary layer strucuture and receptivity. J. Fluid Mech. **281**, 193–218 (1994)